In situ monitoring of surface depressions in metal laser additive manufacturing and its interlayer transfer mechanism

Jie Li[1], Jie Wan[1,2,*], Zijian Chen[1], Jinshan Li[1,2], Jun Wang[1,2,*]

1.State Key Laboratory of Solidification Processing, Northwestern Polytechnical University, Xi'an, Shaanxi 710072, P.R. China
2.Chongqing Innovation Center, Northwestern Polytechnical University, Chongqing, 401120, P.R. China
3.*Correspondence: wan@nwpu.edu.cn (Jie Wan); nwpuwj@nwpu.edu.cn (Jun Wang)
Brief introduction to the first author:
Li Jie, born in 1999, is a doctoral student. Research interest: Formation mechanism of defects in metal additive manufacturing.
Email: jieli647@163.com
Brief introduction to the corresponding author:
Wan Jie, born in 1992, Ph.D., associate professor. Research interest: Laser additive manufacturing of advanced metal materials.
Email: nwpuwj@nwpu.edu.cn
Wang Jun, born in 1984, Ph.D., professor. Research interest: Solidification science and technology.
Email: nwpuwj@nwpu.edu.cn

Abstract: In laser powder bed fusion (LPBF) additive manufacturing, surface depressions caused by melt pool instability can induce defects throughout the layer-by-layer printing process. To address the limited understanding of interlayer defect transmission mechanisms, this study uses synchrotron X-ray in situ imaging to systematically investigate the dynamic evolution of surface depressions during multi-pass printing by adjusting interlayer process parameters. Experimental results show that insufficient energy input in the first layer leads to balling and fracture of melt tracks. When the energy input in the second layer is increased, local overheating at the gap between melt tracks from the previous layer causes surface depressions. Reducing the energy input in the third layer hinders melt backflow, enlarging the depression region. Further lowering the energy input in the final layer leads to the formation of internal unfused defects. This study reveals the dynamic correlation between surface depressions and interlayer defect evolution, offering critical experimental evidence and theoretical guidance for closed-loop interlayer process control in laser additive manufacturing.

Keywords: Laser Powder Bed Fusion; Synchrotron Radiation X-ray Imaging; Cross-layer Defects; Dynamic Regulation

1 Introduction

Laser Powder Bed Fusion (LPBF) additive manufacturing offers significant advantages in achieving integrated material–structure–performance fabrication due to its unique layer-by-layer process. It has been widely applied in high-end sectors such as aerospace and biomedical engineering [1]. However, complex physical phenomena such as melt flow and phase-change heat transfer cause significant fluctuations in melt pool behavior, leading to various porosity defects, including keyholes, gas pores, and lack of fusion [2]. More importantly, the inherent layer-by-layer nature of LPBF allows these defects to propagate vertically, significantly degrading the component's performance, especially its fatigue life [3]. Therefore, understanding melt flow dynamics and their relationship with defect formation is essential for ensuring component quality.

Studies on surface depression defects in melt pools have produced several important findings. Using a three-dimensional transient multiphase model, Pang et al. [4] systematically investigated the effects of environmental pressure and laser power on melt pool morphology. They identified vapor recoil pressure as the main cause of surface depression, with reduced ambient pressure significantly worsening the defect. Zheng et al. [5] found that changes in laser scanning speed and powder layer thickness significantly affect melt pool depression characteristics. High scanning speeds tend to cause periodic depressions at the rear of the melt pool. Ren et al. [6] also reported that insufficient laser energy causes multiple beam reflections among powder particles, leading to uneven energy distribution and the formation of unmelted regions and random surface depressions. Collectively, these studies indicate that surface depressions fundamentally result from external forces causing surface deformation of the melt pool, which, due to rapid solidification, cannot be promptly reflowed to fill the defects. Although optimizing parameters such as laser power and scanning speed can help control melt flow and reduce surface depressions, current studies insufficiently address their impact on the formation quality of subsequent layers.

Investigating the layer-by-layer defect formation process requires advanced characterization techniques. Traditional metallography and X-ray computed tomography (X-CT) can detect final defects but fail to capture their dynamic formation [7]. Although infrared thermography and high-speed imaging provide real-time data on melt pool temperature and surface morphology [5,6], they are limited in penetration depth and resolution [8, 9]. In contrast, synchrotron X-ray imaging enables the study of transient melt pool phenomena with submicron spatial and temporal resolution [10]. Synchrotron X-ray imaging has been widely used to investigate defect formation mechanisms during single-pass printing. Hojjatzadeh et al. [11] identified six types of pores during single-pass printing and revealed their formation mechanisms. Simonds et al. [12] and Zhao et al. [13] captured abnormal keyhole formation at laser start and stop points, respectively. Huang et al. [14] investigated keyhole behavior across stable, unstable, and transitional states. However, single-layer studies often overlook the cumulative effects of interlayer thermal history and surface morphology on subsequent melt pool behavior and defect formation. In recent years, researchers have increasingly focused on defects between multiple layers. Stef et al [15] used X-CT to show that pores often occur at pass junctions. Leung et al. [16] employed synchrotron X-ray imaging to reveal interlayer wetting and growth mechanisms, finding that a thin powder layer between melt tracks easily leads to lack-of-fusion and interlayer porosity. However, the effect of the depression of the melt pool surface on the generation of defects and interlayer transfer was not discussed.

Utilizing the BL12SW beamline at the Shanghai Synchrotron Radiation Facility, this study enables in situ dynamic observation of the LPBF multi-pass printing process. The interlayer transfer of surface depressions under varying energy densities was systematically studied by adjusting process parameters. The depression region significantly influences closed-loop interlayer process control due to increased laser absorption and thermal resistance. This provides critical experimental evidence and theoretical support for achieving high-performance metal additive manufacturing.

2 Experimental Methods

This experiment was conducted at the BL12SW beamline of the Shanghai Synchrotron Radiation Facility. A custom-built micro-printing system was employed, consisting of a laser optics system, atmosphere control, powder spreading module, and synchronized imaging unit. Fig. 1a presents a schematic of the powder spreading system, including the molding piston and sample table (Fig. 1a1), and the powder bin with scraper (Fig. 1a2).

A monochromatic X-ray beam (98.76 keV, 0.1255 Å) passed through a grating slit (0.5 mm × 0.5 mm) to illuminate the sample. The transmitted X-rays were recorded using a high-speed CMOS camera (exposure time: 10 ms, resolution: 2320 × 1031, pixel size: 3 μm). A sandwich-structured sample (Fig. 1b) was prepared, consisting of a 2 mm-thick Ti-6Al-4V substrate positioned between two 1 mm-thick carbon glass plates. The acquired X-ray images were processed using flat-field correction to eliminate artifacts caused by pixel variation and thermal noise during acquisition [16].

The experimental material was gas-atomized Ti-6Al-4V powder (15-53 μm, Xi'an Ouzhong Materials Technology Co., Ltd.). A powder layer thickness of 100 μm was used for each deposition, and the oxygen concentration in the argon atmosphere was maintained below 100 ppm. The substrate was not preheated before printing. By varying laser power and scanning speed, the line energy density ($IED = \frac{P}{V}$, where P is laser power and V is scanning speed) was adjusted to investigate its effects on surface cavity morphology and interlayer defect transmission. The selected printing parameters for each layer are listed in Table 1. The first layer used low energy density to induce melt pool spheroidization, establishing a baseline morphology for subsequent analysis. In the second layer, laser power was increased to investigate the effect of recoil pressure-induced melt pool oscillations on surface cavity formation. In the third layer, energy density was reduced by increasing scanning speed to examine the effect of high-speed melt flow recirculation on surface cavities. In the fourth layer, laser power was significantly reduced, leading to a marked drop in energy input to validate the lack-of-fusion defect formation. This experimental design enabled a systematic investigation of the effects of abrupt energy input changes and melt flow velocity on surface cavity formation.

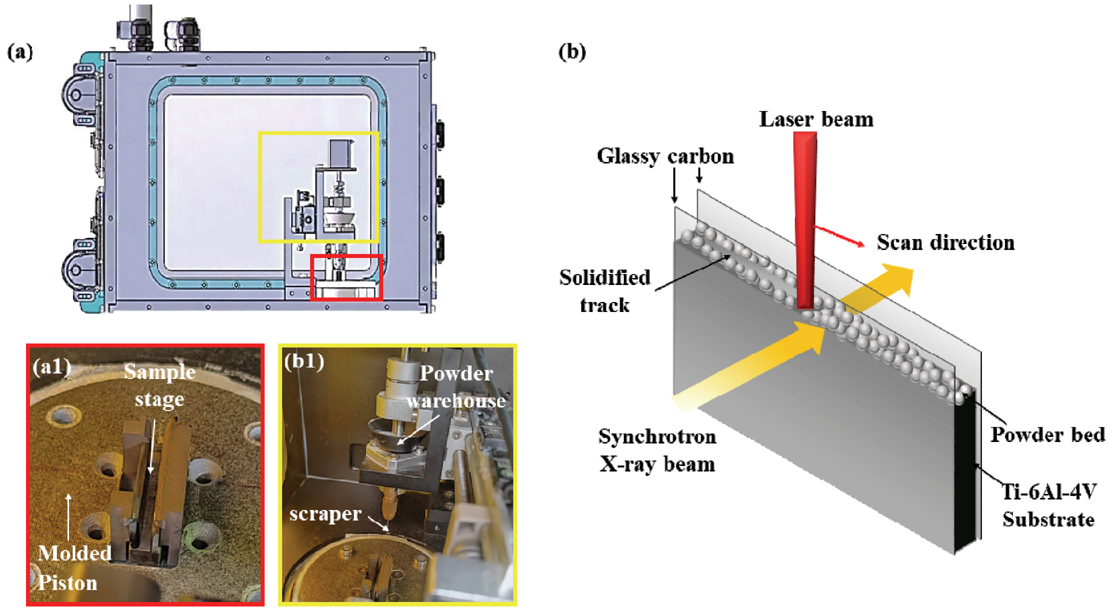

Fig. 1: Schematic diagram of in-situ X-ray characterization of the LPBF additive manufacturing process. (a) Schematic of the powder spreading system; (a1) Sample table lifting system; (a2) Powder delivery and filling device; (b) Schematic of the in-situ X-ray imaging experiment.

Table 1: Process parameters of the in-situ additive manufacturing experiment.

Layer	Powder (W)	Scan Speed (mm·s^{-1})	Line Energy Density (J·mm^{-1})
First layer	75	4	18.75
Second layer	100	4	25
Third layer	100	10	10
Fourth layer	75	10	7.5

3. Results and Discussion

3.1 Surface Dimple Morphology Evolution

3.1.1 Molten Pool Spheroidization (First layer)

Fig. 2 illustrates the dynamic evolution of melt pool morphology during the first-layer printing process, with the laser scanning from right to left. At the initial stage, a low energy input (18.75 J·mm^{-1}) results in balling and cracking of the melt track. Initially, the powder bed exhibits a distinct interface between the substrate and the powder layer (Fig. 2a). After 100 ms of laser irradiation (Fig. 2b), a vapor cavity forms with a depth of 25.1 µm and a width of 69.4 µm, penetrating less than the full powder bed thickness (100 µm). As shown in Fig. 3b, the cavity dimensions decrease (depth: 17.7 µm, width: 42.6 µm), still failing to penetrate the powder bed. After printing, the melt track displays pronounced balling, leading to discontinuous and irregular track formation. Ultimately, the melt track evolves into discrete spherical droplets (Fig. 3d), with an average curvature radius of 85.5 µm and a contact angle of 134°. Under low energy density, poor melt wettability triggers Rayleigh–Plateau instability, causing the melt track to fragment into discrete droplets with prominent surface depressions. These depressions contain numerous partially melted powder particles, further disrupting melt uniformity and hindering thermal conduction in subsequent layers.

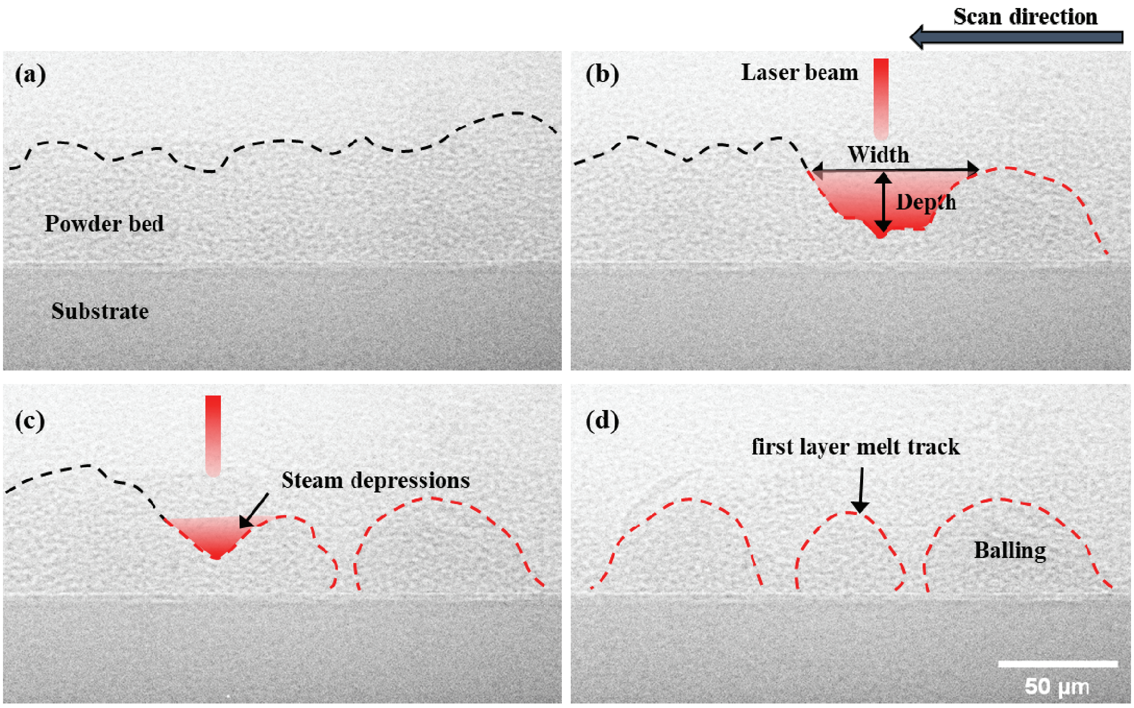

Fig. 2: Morphology evolution of the first-layer melt pool: (a) 0 ms; (b) 100 ms; (c) 200 ms; (d) 300 ms. (The black lines represent the powder bed interface, while the red lines indicate the interface of the solidified melt channel.)

3.1.2 Surface Depressions under High Power (Second layer)

To compensate for the insufficient energy input in the first layer, the second layer employed an active control strategy by increasing the laser power, raising the energy density to 25 J·mm^{-1} (a 33% increase). This adjustment aimed to investigate the effect of melt pool oscillations on surface depressions under elevated recoil pressure, while maintaining the powder layer thickness at 100 μm. Fig. 3a shows a shallow vapor cavity (depth 45.3 μm, width 60.2 μm). After 50 ms (Fig. 3b), the vapor cavity expands at the balling gap of the first layer, reaching a width of 85.3 μm and a depth of 120.5 μm. At 100 ms (Fig. 3c), the vapor cavity deepens further and penetrates the substrate, with the width narrowing to 70.2 μm and the shape becoming more elongated. Fig. 3d shows the melt track morphology after the second-layer printing, revealing a depression formed between the balling droplets of the first layer, with a depth of 324 μm, a width of 78 μm, and tilt angles of 49.3° (left) and 60.9° (right). Measurements indicate that the actual powder thickness at the depression site (Fig. 3d) is approximately 182 μm, significantly exceeding the nominal 100 μm, thereby increasing the local powder volume requiring melting. The thermal resistance in thicker powder regions is significantly higher than in thinner ones[17], which impedes heat dissipation and leads to localized heat accumulation. Local overheating triggers intense material vaporization, where recoil vapor pressure surpasses the melt's surface tension, leading to the formation of surface depressions in the melt track[18].

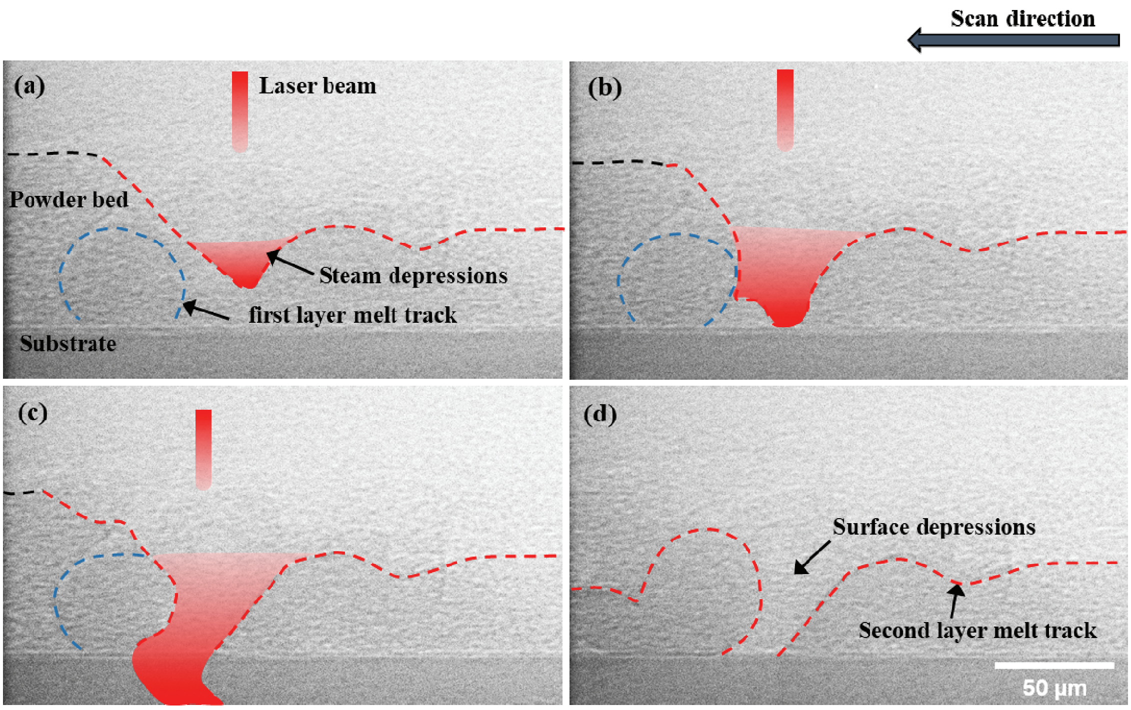

Fig. 3: Morphological evolution of the second-layer melt pool: (a) 0 ms; (b) 50 ms; (c) 100 ms; (d) 250 ms. (The black line is the powder bed interface, the blue line is the surface of the first layer of the melt channel, and the red line is the surface of the second layer of the melt channel.)

3.1.3 Surface depressions at high scanning rates (Third layer)

In the third layer, the scanning speed was increased, reducing the energy density to 10 J·mm^{-1}. As a result, a wide and shallow concave cavity with a narrow tip formed 82 μm to the upper left of the deep pit created in the second layer (scanning direction: right to left), as shown in Fig. 4. The initial powder layup revealed a powder thickness of 96 μm in the concave region (Fig. 4a). After 50 ms of laser irradiation (Fig. 4b), a narrow depression with a depth of 94.2 μm appeared in the P1-P2 region. At 100 ms (Fig. 4c), the surface depression widened further, and the depth slightly increased above the P2-P3 gap, although it remained significantly less than that above the P1-P2 gap. Fig. 4d shows the final morphology of the melt track in the third layer, featuring a concave cavity with a depth of 164 μm and width of 266 μm, and front and rear inclination angles of 74.9° and 71.8°, respectively.

The formation of this irregularly wide and shallow cavity is due to the difference in thermal resistance between thick and thin powders. Higher thermal resistance in thick powder regions intensifies local heat accumulation, potentially forming deep melt zones or even keyholes [14], thereby increasing surface concavity. This effect manifests as the narrow depression between P1 and P2 in Fig. 4d. In contrast, when the laser traverses a thin powder region, the sudden drop in thermal resistance causes rapid cooling of the melt pool. This leads to a shallower penetration depth, increased melt viscosity, and inhibited backflow, ultimately forming a wide concave cavity with a narrow tip. The leftward shift of the third-layer surface depression results from the combined effects of Marangoni convection and changes in melt wetting direction induced by the second-layer depression (a negatively curved surface) [19]. The capillary suction generated by the sidewalls of the second layer surface depression attracts the melt to flow to the left (against the scanning direction), resulting in a shift of the melt pool center relative to the laser spot position.

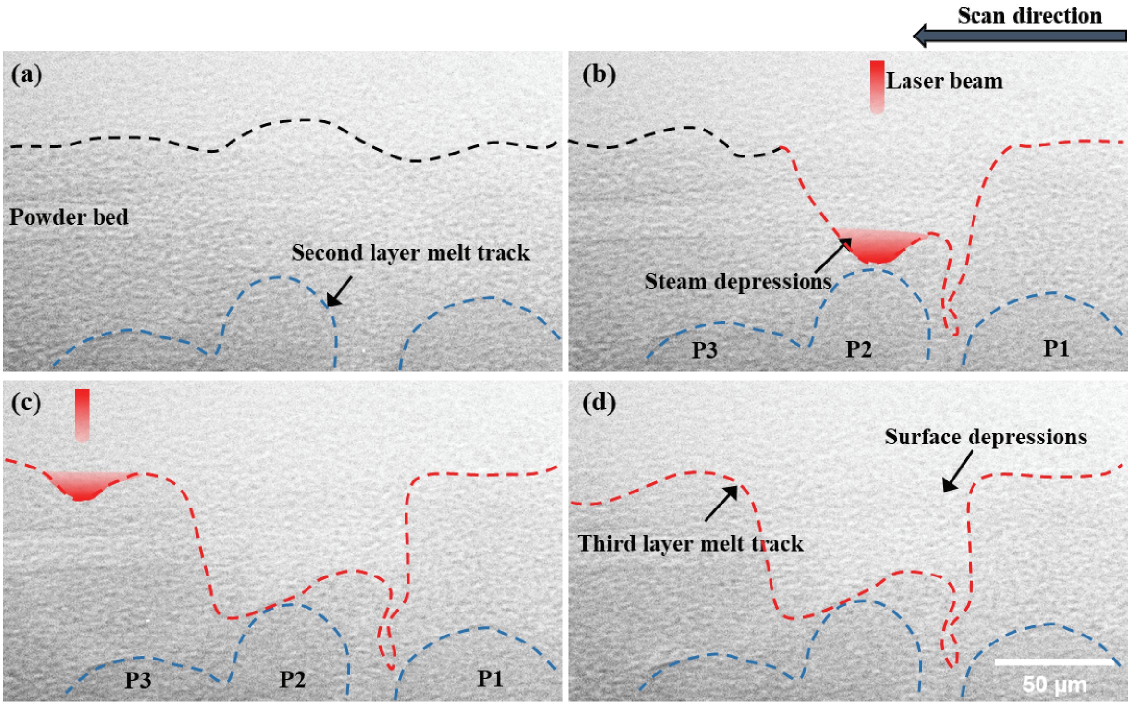

Fig. 4: Morphological evolution of the third-layer melt pool: (a) 0 ms; (b) 50 ms; (c) 100 ms; (d) 150 ms. (The black line is the powder bed interface, the blue line is the surface of the second layer of the melt channel, and the red line is the surface of the third layer of the melt channel.)

3.1.4 Lack of fusion defects (fourth layer)

Although the energy input was reduced in the third layer, it was further decreased in the fourth layer to 7.5 $J{\cdot}mm^{-1}$ to examine defect evolution resulting from the pores formed previously. In-situ observations revealed the formation of lack-of-fusion defects above the surface depression of the third layer and within the fourth layer. As shown in Fig. 5a, the melt pool exhibits a shallow bowl-like shape, with its base initially contacting the depression area of the third layer. At 30 ms (Fig. 5b), the melt pool fails to fully cover the depression zone, leading to the emergence of a triangular lack-of-fusion defect with an area of 403.5 μm², which is consistent with typical geometric characteristics of such defects. By 60 ms (Fig. 5c), the defect expands to 612.8 μm², evolving into a distinctive "swallow-tail" shape. According to the Rosenthal melting depth model [20], the melt pool depth DD is estimated as: $d = \frac{AP}{k(T_m - T_0)\sqrt[3]{V}}$, where d is the depth of the melt pool, P is the laser power (75 W), k is the thermal conductivity (6.7 $W{\cdot}(m{\cdot}K)^{-1}$), T_m is the melting point (1923 K), T_0 is the preheating temperature (298 K), V is the scanning speed (10 $mm{\cdot}s^{-1}$), and A is the modification factor (0.04). Based on these parameters, the melt pool depth was estimated to be 27.5 μm. However, due to the extremely low energy input in the fourth layer, the melt pool failed to penetrate the localized powder layer, which was up to 234 μm thick (including pit-filled powder). It also struggled to melt the newly spread powder above the depression. Consequently, a sharp triangular lack-of-fusion defect inevitably formed within the depression zone, approximately 190 μm below the surface (Fig. 5d).

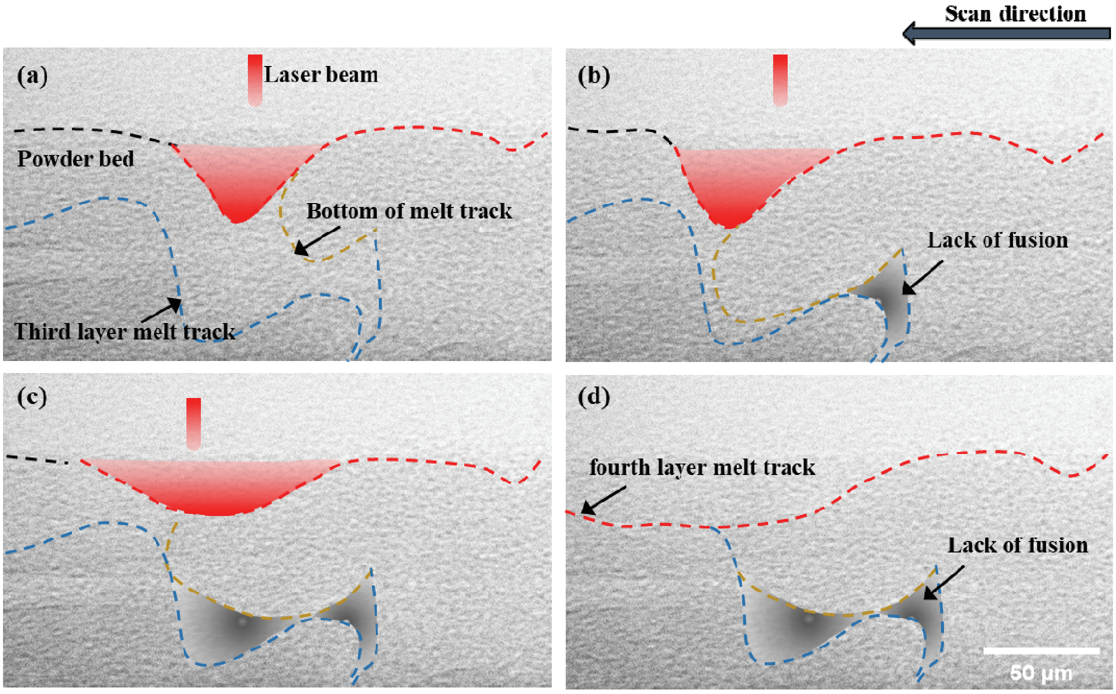

Fig. 5: Morphological evolution of the fourth-layer melt pool: (a) 0 ms; (b) 30 ms; (c) 60 ms; (d) 90 ms. (The black line is the powder bed interface, the blue line is the surface of the third layer of the melt channel, the red line is the surface of the fourth layer of the melt channel, amd the yellow line is the bottom of the fourth layer of the melt channel.)

3.2 Cross-layer transfer mechanism of pore defects

Fig.6 illustrates the interlayer transition process during layer-by-layer printing under varying energy inputs. This transition progresses from melt pool spheroidization to narrow surface depressions, to wide and shallow concave cavities, and ultimately to lack-of-fusion defects. The evolution is primarily driven by abrupt changes in energy input, coupled with surface irregularities.

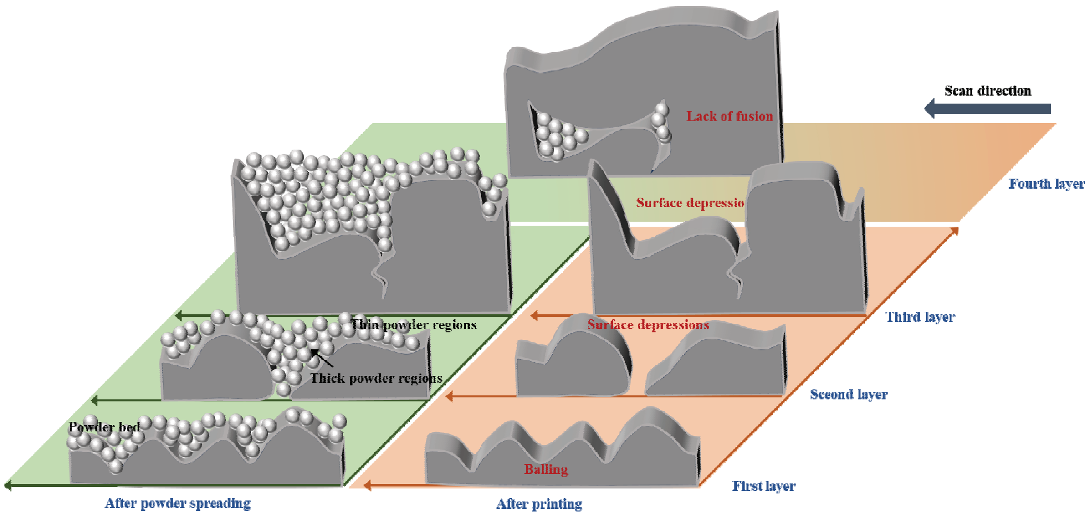

Fig. 6: The morphology of melt tracks and surface depressions after completion of printing from the first to fourth layers.

Variations in powder layer thickness on irregular surfaces can distort the local temperature field of the melt pool. Thick powder regions from the previous layer (e.g., spheroidization gaps or concave cavities) exhibit higher thermal resistance and greater laser absorption than thin powder regions [21]. Localized overheating in thick powder regions hinders heat dissipation, resulting in deeper melt pools. In contrast, in shallow powder regions, reduced laser absorption accelerates melt pool solidification and limits penetration depth, increasing the risk of lack-of-fusion defects. Intrinsic laser fluctuations lead to inherent surface irregularities on the melt track [22]. Consequently, subsequent powder layers exhibit periodic variations between thick and thin regions, causing surface morphology fluctuations in the printed layers. Under low energy input, these fluctuations are exacerbated by spheroidized and fragmented melt tracks. Under active control, increasing the energy input in the next layer deepens the melt pool, which interacts with the underlying geometric features and further degrades surface quality. Conversely, when energy input is actively reduced, and the melt pool still penetrates the powder layer, surface depressions can still form in thick powder regions. If the melt pool fails to penetrate the powder layer, unmelted powder in surface depressions results in internal lack-of-fusion defects. Notably, variations in the radius of curvature of surface depressions alter the melt wetting direction. Capillary forces generated by the depression sidewalls draw the melt backward (against the scanning direction), causing a shift in the melt pool position.

4. Conclusions

This study employed in situ synchrotron X-ray imaging to investigate the mechanisms underlying interlayer defect evolution induced by parameter variations in laser powder bed fusion (LPBF). The key findings are summarized as follows:

(1) Variations in interlayer energy input govern defect morphology evolution. Low energy input in the initial layer leads to spheroidized surface features. Subsequent increases in energy cause localized overheating and surface depressions. In the third layer, high scanning speed restricts melt flow, enlarging the depressions. Reduced power in the final layer leaves residual porosity within these depressions.

(2) Coupling of energy mutations and interlayer morphology governs defect propagation: Variations in thermal resistance and laser absorption between thick and thin powder regions cause distortions in the temperature field. This leads to localized overheating in thick powder areas, increasing melt pool depth, and resulting in surface depressions.

(3) Surface morphology influences melt wetting behavior. Capillary forces from the sidewalls of surface depressions redirect melt flow opposite to the scanning direction, causing the melt pool to shift. As a result, surface depressions gradually migrate along the scanning path.

Disclosure statement

No potential conflict of interest was reported by the author(s).

Data availability

The raw data are available from the corresponding author upon reasonable request.

Acknowledgements

This work was supported by the National Key Research and Development Program of China (No. 2022YFB3707103); the Natural Science Foundation of Chongqing, China (No. CSTB2022NSCQ-MSX0945); the Fundamental Research Funds for the Central Universities (No. D5000240144) and the Young Talent Fund of Xi'an Association for Science and Technology (No. 959202413014).

References

[1] Gu D, Shi X, Poprawe R, et al. Material-structure-performance integrated laser-metal additive manufacturing. Science, 2021, 372(6545): 1-15.
[2] Niu Z, He C, Yang Z, et al. Dynamics of molten droplet/pool fusion in additive manufacturing. Acta Mech. Sin., 2025, 42(3): 325020.
[3] Javidrad H, Bahattin K, Hakan B, et al. Fatigue performance of metal additive manufacturing: a comprehensive overview. Virtual Phys. Prototyp., 2024, 19(1): 5-22.
[4] Pang S, Chen X, Zhou J, et al. 3D transient multiphase model for keyhole, vapor plume, and weld pool dynamics in laser welding including the ambient pressure effect. Opt. Laser Eng., 2015, 74: 47-58.
[5] Zheng M, Wei L, Chen J, et al. A novel method for the molten pool and porosity formation modelling in selective laser melting. Int. J. Heat Mass Transf., 2019, 140: 1091-1105.
[6] Wang C H, Fu S Y, Kung L J, et al. Combustion and microexplosion of collision-merged methanol/alkane droplets. Proc. Combust. Inst., 2005, 30(2): 1965-1972.
[7] Ziabari A, Venkatakrishnan S V, Snow Z, et al. Enabling rapid X-ray CT characterisation for additive manufacturing using CAD models and deep learning-based reconstruction. NPJ Comput. Mater., 2023, 9(1): 91.
[8] Myers A J, Quirarte G, Beuth J L, et al. Two-color thermal imaging of the melt pool in powder-blown laser-directed energy deposition. Addit. Manuf., 2023, 78(25): 103855.
[9] Bidare P, Bitharas I, Ward R M, et al. Fluid and particle dynamics in laser powder bed fusion. Acta Mater., 2018, 142: 107-120.
[10] Khairallah S A, Martin A A, Lee J R I, et al. Controlling interdependent meso-nanosecond dynamics and defect

generation in metal 3D printing. Science, 2020, 368(6491): 660-665.

[11] Hojjatzadeh S M H, Parab N D, Guo Q, et al. Direct observation of pore formation mechanisms during LPBF additive manufacturing process and high energy density laser welding. Int. J. Mach. Tool Manuf., 2020, 153: 103555.

[12] Simonds B J, Tanner J, Artusio-Glimpse A, et al. The causal relationship between melt pool geometry and energy absorption measured in real time during laser-based manufacturing. Appl. Mater. Today, 2021, 23: 101049.

[13] Zhao C, Fezzaa K, Cunningham R W, et al. Real-time monitoring of laser powder bed fusion process using high-speed X-ray imaging and diffraction. Sci. Rep., 2017, 7: 3602.

[14] Huang Y, Fleming T G, Clark S J, et al. Keyhole fluctuation and pore formation mechanisms during laser powder bed fusion additive manufacturing. Nat. Commun., 2022, 13(1): 1170.

[15] Stef J, Poulon-Quintin A, Redjaimia A, et al. Mechanism of porosity formation and influence on mechanical properties in selective laser melting of Ti-6Al-4V parts. Mater. Des., 2018, 156: 480-493.

[16] Leung C L A, Marussi S, Atwood R C, et al. In situ X-ray imaging of defect and molten pool dynamics in laser additive manufacturing. Nat. Commun., 2018, 9: 1355.

[17] Gusarov A V, Yadroitsev I, Bertrand P, et al. Heat transfer modelling and stability analysis of selective laser melting. Appl. Surf. Sci., 2007, 254(4): 975-979.

[18] Calta N P, Wang J, Kiss A M, et al. An instrument for in situ time-resolved X-ray imaging and diffraction of laser powder bed fusion additive manufacturing processes. Rev. Sci. Instrum., 2018, 89(5): 055101.

[19] Khairallah S A, Anderson A T, Rubenchik A, et al. Laser powder-bed fusion additive manufacturing: Physics of complex melt flow and formation mechanisms of pores, spatter, and denudation zones. Acta Mater., 2016, 108: 36-45.

[20] King W E, Anderson A T, Ferencz R M, et al. Laser powder bed fusion additive manufacturing of metals; physics, computational, and materials challenges. Appl. Phys. Rev., 2015, 2(4): 610-644.

[21] Yan S P, Zhang A F, Liang S D, et al. Measurement of laser absorptivity of common metal materials used in laser additive manufacturing technology. Aeronaut. Manuf. Technol., 2017, (17): 97-100.

[22] Ren Z, Gao L, Clark S J, et al. Machine learning-aided real-time detection of keyhole pore generation in laser powder bed fusion. Science, 2023, 379(6627): 89-94.